JACS
JOURNAL OF THE AMERICAN CHEMICAL SOCIETY
Article
pubs.acs.org/JACS

Visible Light Driven Benzyl Alcohol Dehydrogenation in a Dye-Sensitized Photoelectrosynthesis Cell

Wenjing Song,[†] Aaron K. Vannucci,[†] Byron H. Farnum,[†] Alexander M. Lapides,[†] M. Kyle Brennaman,[†] Berç Kalanyan,[§] Leila Alibabaei,[†] Javier J. Concepcion,[†,‡] Mark D. Losego,[§] Gregory N. Parsons,[§] and Thomas J. Meyer*[,†]

[†]Department of Chemistry, University of North Carolina at Chapel Hill, CB3290, Chapel Hill, North Carolina 27599, United States
[§]Department of Chemical and Biomolecular Engineering, North Carolina State University, Raleigh, North Carolina 27695, United States

Supporting Information

ABSTRACT: Light-driven dehydrogenation of benzyl alcohol (BnOH) to benzaldehyde and hydrogen has been shown to occur in a dye-sensitized photoelectrosynthesis cell (DSPEC). In the DSPEC, the photoanode consists of mesoporous films of TiO_2 nanoparticles or of core/shell nanoparticles with tin-doped In_2O_3 nanoparticle (nanoITO) cores and thin layers of TiO_2 deposited by atomic layer deposition (nanoITO/TiO_2). Metal oxide surfaces were coderivatized with both a ruthenium polypyridyl chromophore in excess and an oxidation catalyst. Chromophore excitation and electron injection were followed by cross-surface electron-transfer activation of the catalyst to $-Ru^{IV}=O^{2+}$, which then oxidizes benzyl alcohol to benzaldehyde. The injected electrons are transferred to a Pt electrode for H_2 production. The nanoITO/TiO_2 core/shell structure causes a decrease of up to 2 orders of magnitude in back electron-transfer rate compared to TiO_2. At the optimized shell thickness, sustained absorbed photon to current efficiency of 3.7% was achieved for BnOH dehydrogenation, an enhancement of ~10 compared to TiO_2.

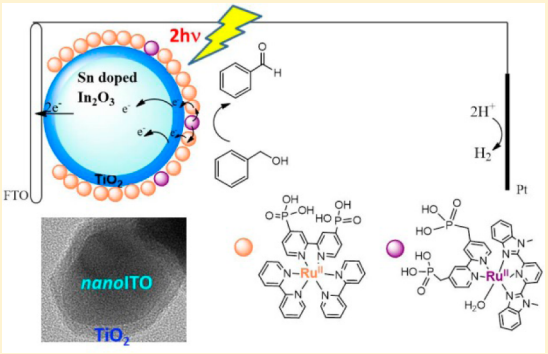

INTRODUCTION

In artificial photosynthesis the goal is to store solar energy in the bonds of high-energy molecules, "solar fuels".[1−5] Recently, visible light splitting of water into hydrogen and oxygen was reported in dye-sensitized photoelectrosynthesis cells (DSPEC).[6−11] In a DSPEC, molecular level light absorption and catalysis are integrated with wide band gap n-type semiconductors. Water oxidation catalysis is initiated by molecular-level light absorption and electron injection into the conduction band of the semiconductor followed by electron-transfer activation of the catalyst.[1,2,10] Ruthenium polypyridyl water oxidation catalysts are appealing in this role given their extensive and well-developed catalytic oxidation chemistry which has been extended to the surfaces of metal oxide conductors and semiconductors.[12,13] The chemistry is based on proton coupled electron transfer (PCET) oxidative activation of $-Ru^{II}$ aqua precursor complexes to high oxidation state intermediates $-Ru^{IV}=O^{2+}$, $-Ru^{IV}(OH)^{3+}$, $-Ru^{V}(O)^{3+}$, and $-Ru^{V}(OO)^{3+}$, which are active toward O atom transfer, H atom transfer, hydride transfer, and C−H insertion.[14,15]

In a recent paper we reported that activation of the water oxidation catalyst [Ru(Mebimpy)((4,4′-$(OH)_2PO$-$CH_2)_2$bpy)-(OH_2)]$^{2+}$ ($\mathbf{Ru^{II}OH_2^{2+}}$, Mebimpy = 2,6-bis(1-methylbenzimidazol-2-yl)pyridine, (4,4′-$(OH)_2PO$-$CH_2)_2$bpy) = 4,4′-bismethlylenephosphonato-2,2′-bipyridine) to $-Ru^{IV}=O^{2+}$ occurred under steady-state photolysis conditions on surfaces of TiO_2 photoanodes co-loaded with the chromophore, [Ru-$(bpy)_2$((4,4′-$(OH)_2PO)_2$bpy)]$^{2+}$ ($\mathbf{Ru^{II}P^{2+}}$, bpy = 2,2′-bipyridine, (4,4′-$(OH)_2PO)_2$-bpy = 2,2′-bipyridine-4,4′-diyldiphosphonic acid).[16] In the current study we exploit this earlier observation and utilize the surface-bound $-Ru^{IV}=O^{2+}$ form of the catalyst to demonstrate light-driven oxidation of benzyl alcohol (BnOH) to benzaldehyde with hydrogen generation at the Pt cathode in a DSPEC. The net reaction is shown in eq 1. This result is directly related to an earlier report on the photodehydrogenation of isopropanol to acetone[17] and to other photocatalytic systems[18−22] reported for BnOH dehydrogenation.

$$PhCH_2OH \xrightarrow{h\nu} PhCHO + H_2 \quad (1)$$

Accumulation of multiple redox equivalents for catalyst activation is essential in both solar-driven water splitting and C−H functionalization reactions in order to avoid high-energy 1e$^-$ intermediates.[2,11,16,23−25] The $pK_{a,1}$ values for the $-Ru^{II}-OH_2^{2+}$, $-Ru^{III}-OH_2^{3+}$, and $-Ru^{IV}(OH)^{3+}$ forms of the catalyst are 11.5, 2.5, and 3.2 in aqueous solution.[14,26] Oxidation of $-Ru^{II}-OH_2^{2+}$ gives $-Ru^{IV}=O^{2+}$ with added bases facilitating

Received: May 19, 2014
Published: June 16, 2014

   dx.doi.org/10.1021/ja505022f | J. Am. Chem. Soc. 2014, 136, 9773−9779

the loss of protons in the successive oxidation to $-Ru^{III}-OH^{2+}$ and to $-Ru^{IV}=O^{2+}$.[14,26,27] The concentration, nature of the buffer base and pH also play important roles in catalysis.[26−28]

An additional complication arises from the competition between injection/oxidative activation of the catalyst and back electron transfer.[6,11,29−31] In a DSSC, loss of efficiency by back electron transfer between $TiO_2(e^-)$ and the oxidized form of redox active electrolytes such as I_3^-/I^- occurs on the ms to s time scale.[32−35] In a DSPEC for multielectron solar fuel half reactions, high-energy oxidative equivalents (holes) must be accumulated at surface catalyst sites which undergo recombination with injected electrons on the μs to ms time scale.[32,36] Under ambient sunlight the rate of solar insolation is only 1−2 s^{-1} and catalytic reactions are relatively slow (10^{-2}−10^2 s^{-1}).[12−14,37−40] With these competitive interfacial dynamics, the ability to accumulate multiple redox equivalents on photoelectrode surfaces is limited.

Recently we reported a novel, high surface area core/shell structured material consisting of a core of tin-doped In_2O_3 nanoparticles (nanoITO) and a TiO_2 shell (nanoITO/TiO_2). In a DSSC application based on nanoITO/TiO_2 core/shells derivatized with the N719 dye ($[N(n\text{-}C_4H_9)_4]_2[cis\text{-}Ru(4,4'\text{-}(CO_2^-)(bpy)_2(NCS)_2)]$, the core/shell structure exhibited shell thickness-dependent back electron-transfer dynamics and DSSC performance.[41] Successful solar water splitting was similarly demonstrated in a DSPEC with a chromophore-catalyst derivatized nanoITO/TiO_2 photoanode.[42] We demonstrate here that the use of the core/shell structural motif significantly inhibits back electron transfer at a coderivatized photoanode, resulting in an efficiency enhancement of ∼10 compared to TiO_2 for BnOH dehydrogenation to benzaldehyde and hydrogen.

EXPERIMENTAL SECTION

Materials. Aqueous solutions were prepared from water purified by a Millipore Milli-Q Synthesis A10 purification system. Lithium perchlorate (99.999% trace metal basis), 70% perchloric acid (99.999%), lithium acetate (99.99%), benzyl alcohol (99.5%) (BnOH), titanium isopropoxide, and isopropanol were used as received from Sigma-Aldrich. Glacial acetic acid, methanol, and ethanol were obtained from Fisher Scientific. Sn-doped In_2O_3 (ITO) nanoparticle powder was purchased from Lihochem. $Ru^{II}P^{2+}$ and $Ru^{II}OH_2^{2+}$ were synthesized according to previously published procedures.[37,43]

TiO_2 and nanoITO Mesoporous Film Preparation. Anatase TiO_2 (15−20 nm nanopoarticles) paste was prepared according to a reported literature procedure.[44] The paste was doctor bladed on top of FTO (fluorine-doped SnO_2, sheet resistance 15 Ω, Hartford Glass Co. Inc.) and annealed under air at 450 °C for 30 min.

Three grams of nanoITO powder was added to a mixture of 3 g of acetic acid and 10 mL of ethanol giving a 5 M solution. The colloidal suspension was sonicated for 20 min followed by ultrasonication with a Branson ultrasonic horn flat microtip (70% power, 50% duty cycle; 5 min). The nanoITO colloidal suspension was coated on the FTO glass substrate by a spin-coater at 600 rpm. Thin films were annealed in two steps: (1) 500 °C in air followed by and (2) 300 °C under H_2/N_2 gas.[45]

Atomic Layer Deposition (ALD). A custom-built, hot walled, flow tube reactor or a Savannah ALD system from Cambridge Nanotech (Cambridge, MA) was used for the deposition of TiO_2. The thickness of the outer shell of TiO_2 was controlled by the number of deposition cycles. The shell thickness was measured by transmission electron microscopy (TEM) on a JEOL 2010F FasTEM. Precursors used were 99% pure $TiCl_4$ (Strem Chemicals) for 50 cycles deposition in the custom built ALD systems or tetrakis(dimethylamido)titanium (TDMAT) (Sigma-Aldrich) for 30 and 70 cycles deposition in the Savannah ALD system. ALD coating details were given in Supporting Information.

Measurements. TiO_2 and nanoITO/TiO_2 films were derivatized by soaking in a 50−100 μM $Ru^{II}P^{2+}$ methanol solution, followed by a 50−100 μM $Ru^{II}OH_2^{2+}$ methanol solution. Surface coverage of each complex (Γ in mol cm^{-2}) was determined from Beer's Law as described previously.[16]

Transient absorption (TA) measurements were carried out by inserting derivatized TiO_2 or nanoITO/TiO_2 films at a 45° angle into a standard 10 mm path length square Pyrex cuvette containing electrolyte. The top of the cuvette was fit with an O-ring seal with a Kontes valve inlet to allow the contents to be purged with Argon. The experiments were performed by using nanosecond laser pulses produced by a Spectra-Physics Quanta-Ray Lab-170 Nd:YAG laser combined with a VersaScan OPO (5−7 ns, operated at 1 Hz, beam diameter 1 cm) integrated into a commercially available Edinburgh LP 920 laser flash photolysis spectrometer system (time resolution 10 ns). A white light probe was generated by a pulsed 450 W Xe lamp. The probe light was passed through a 380 nm long pass filter before reaching the sample to avoid direct band gap excitation of TiO_2 and then detected by a photomultiplier tube (Hamamatsu R928). Appropriate color filters were placed before the detector to reject unwanted scattered light. Single wavelength kinetic data were averaged over 50−100 laser shots.

A customized three-arm cell was employed in the electrochemical and photoelectrochemical measurements. The arm for the photoanode was a 10 mm path length Pyrex glass cuvette. A platinum wire was used as the cathode and Ag/AgCl as the reference electrode. The photoanode was inserted at a 45° angle into a homemade Teflon seat located in the cuvette part of the cell. The supporting electrolyte was 20 mM pH 4.5 acetate buffer with 0.1 M $LiClO_4$ unless otherwise specified. Experiments were carried out under argon at (22 ± 2) °C. Illumination for steady-state photoelectrolysis was provided by a Lumencor spectral light engine (λ_{max} = 445 nm, fwhm ∼20 nm, output ∼1.7−83 mW). The light source was integrated with a Newport optical fiber and a focusing/imaging beam probe. The irradiation beam diameter was 10 mm. Photoelectrochemical measurements were performed by combining the light source, a CH Instruments 601D potentiostat, and an Agilent Cary 50 UV−vis spectrophotometer.

Product Analysis. After PEC experiments, headspace gas was withdrawn for GC analysis with a gastight syringe. The headspace gas sample was injected to a PC-interfaced GC (Varian 450-GC) equipped with a 5 Å molecular sieve column and pulsed discharge helium ionization detector (PDHID) plumbed with ultrahigh-purity helium carrier gas (National Welders). Evolved hydrogen was quantified relative to pre-injected methane as internal standard.

For benzaldehyde, GC analyses were performed on a Shimadzu GC-2014 capable of liquid injections with a DB-Wax column. Column temperatures began at 40 °C and were ramped to 220 °C at a rate of 15 °C/min. Extraction of products from bulk electrolysis solutions (5 mL) was performed by using chloroform (3 mL). Standard solutions of benzaldehyde in chloroform were prepared in the same way.

RESULTS

Mesoporous films of nanoITO (3.2 μm) were coated with TiO_2 by 30, 50, and 70 cycles of ALD (Supporting Information). High-resolution transmission electron microscopy (HR-TEM) images of the nanoITO/TiO_2 samples demonstrated a conformal coating of an amorphous TiO_2 shell on the nanoITO cores. The thicknesses of the TiO_2 shells were about 2.0, 3.3, and 4.0 nm by 30, 50, and 70 deposition cycles (Figure 1).

Nanosecond TA measurements were used to investigate interfacial electron-transfer dynamics on $-Ru^{II}P^{2+}$ derivatized TiO_2 and nanoITO/TiO_2 in pH 4.5 acetate/acetic acid buffer with 0.1 M in $LiClO_4$. Injection efficiencies following excitation of $-Ru^{II}P^{2+}$ (eqs 2 and 3) were determined by absorbance changes at 400 nm, the isosbestic point between $Ru^{II}P^{2+}$ ground and excited states.[46] Results are summarized in Table 1. The

dx.doi.org/10.1021/ja505022f | J. Am. Chem. Soc. 2014, 136, 9773−9779

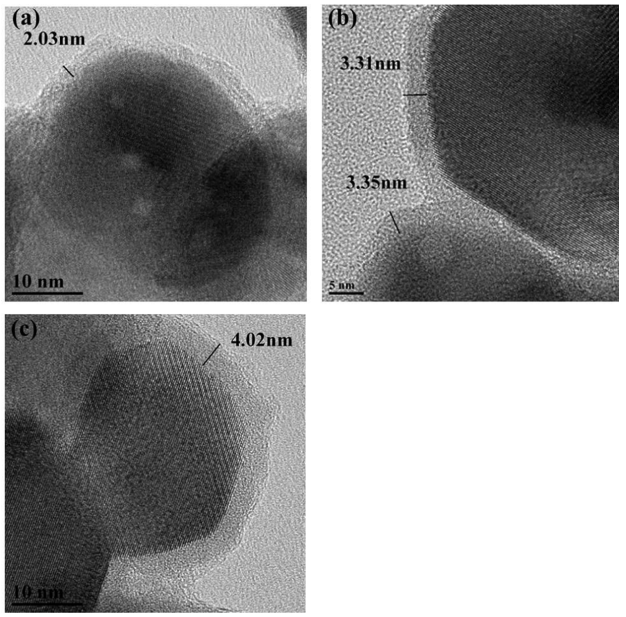

Figure 1. HR-TEM of nanoITO/TiO_2 showing the amorphous TiO_2 layer coated on nanoITO cores by (a) 30 (b) 50 and (c) 70 cycles of ALD deposition.

Table 1. Summary of Photophysical Data for $-Ru^{II}P^{2+}$ on TiO_2 and nanoITO/TiO_2 by Nanosecond TA Measurements

	shell thickness (nm)	injection efficiency[a]	$t_{1/2}$[b] (μs)
TiO_2		0.7	6.1
nanoITO/TiO_2 (30)[c]	2.0	0.27	95
nanoITO/TiO_2 (50)	3.3	0.17	220
nanoITO/TiO_2 (70)	4.0	0.18	350

[a] $TiO_2-Ru^{II}P^{2+}$ in 0.1 M $HClO_4$ was used as the actinometer; 532 nm excitation with absorbance monitoring at 400 nm.[46] [b] Time for half of the absorbance change to occur as calculated from absorbance−time curves by fitting the data to a triexponential decay function. [c] Number of ALD cycles in parentheses.

injection efficiency reached 27% for nanoITO with a 2.0 nm-thick TiO_2 shell and then leveled off to ∼17% and 18% for 3.3 and 4.0 nm TiO_2 shells. These values were lower than for $TiO_2-Ru^{II}P^{2+}$ (70%). The origin of the decreased core/shell injection efficiencies is currently under investigation. Emission quenching is nearly complete, and the decrease appears to result from a rapid back electron-transfer component on the sub-10 ns time scale which might play a larger role for the core/shell structure.

$$TiO_2-Ru^{II} \xrightarrow{h\nu} TiO_2-Ru^{II}* \rightarrow TiO_2(e^-)-Ru^{III} \quad (2)$$

$$\text{nanoITO}/TiO_2-Ru^{II} \xrightarrow{h\nu} \text{nanoITO}/TiO_2-Ru^{II}* \rightarrow \text{nanoITO}(e^-)/TiO_2-Ru^{III} \quad (3)$$

Back electron-transfer dynamics were monitored at 400 nm. Normalized absorbance−time profiles for TiO_2 and nanoITO/TiO_2 are shown in Figure 2. Given the complexity of the kinetics,[41] they were characterized as the time for one-half of the absorbance decay to occur, $t_{1/2}$ (Table 1). Following excitation and injection, back electron transfer on TiO_2 (eq 4) showed a $t_{1/2}$ of 6.1 μs with 90% completed within 10 μs. For nanoITO/TiO_2, $t_{1/2}$ increased from 95 μs to >200 μs as the

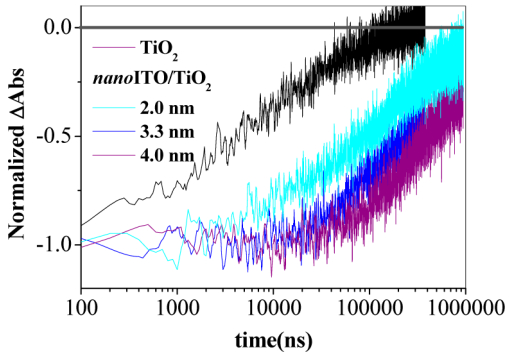

Figure 2. TA changes monitored at 400 nm for RuP^{2+} derivatized TiO_2 (black) and nanoITO/TiO_2 with 2.0 nm (cyan), 3.3 nm (blue) and 4.0 nm (purple) outer shells following 532 nm laser excitation. TiO_2 or nanoITO/TiO_2 films were immersed in 20 mM pH 4.5 acetate aqueous solution with 0.1 M $LiClO_4$ at room temperature.

shell thickness increased from 2.0 to 3.3 nm. For the 4.0 nm shell, $t_{1/2}$ was 350 μs.

As reported for nanoITO/TiO_2-N719,[41] with thinner shells, electron injection appears to occur directly into the nanoITO core, where it is transiently "trapped". Under this condition, back electron transfer is dominated by electron tunneling through the TiO_2 shell (eq 5a). With the 3.3 and 4.0 nm shells, direct injection to the core and injection into TiO_2 trap states in the amorphous shell compete. Back electron transfer occurs both by tunneling (eq 5a) and electron transport in the TiO_2 shell (eq 5b).

The 1-2 magnitude increase in lifetime of the injected electrons on nanoITO/TiO_2 has been attributed to the TiO_2 shell acting as a "blocking" layer increasing the tunneling distance for back electron transfer or to significantly decreased electron diffusion due to the amorphous, noncrystalline nature of TiO_2 shell.[47−51] The pronounced thickness dependence of the outer shell on back electron transfer is especially notable in the context of maximizing efficiencies in potential DSPEC applications where, as noted above, there is a requirement for building up multiple redox equivalents.

$$TiO_2(e^-) - Ru^{III} \rightarrow TiO_2-Ru^{II} \quad (4)$$

$$\text{nanoITO}(e^-)/TiO_2-Ru^{III} \rightarrow \text{nanoITO}/TiO_2-Ru^{II} \quad (5a)$$

$$\text{nanoITO}/TiO_2(e^-)-Ru^{III} \rightarrow \text{nanoITO}/TiO_2-Ru^{II} \quad (5b)$$

The performance of DSPECs toward BnOH oxidation was evaluated on TiO_2 photoanodes derivatized with $Ru^{II}P^{2+}$, $Ru^{II}OH_2^{2+}$, or both, with a $Ru^{II}P^{2+}$: $Ru^{II}OH_2^{2+}$ surface ratio of 8.5:1. Typical current−time profiles in the pH 4.5 buffer with a 0.2 V applied bias vs NHE are shown in Figures 3, S1 and S2. Initial photocurrent spikes were observed for all three cells upon 445 nm irradiation with photocurrents arising from surface photo-oxidation to $-Ru^{III}P^{3+}$, $-Ru^{III}-OH^{2+}$, and/or $-Ru^{IV}=O^{2+}$ (Figures 3a insert, S1 and S3).

From the results of the previous study on co-loaded TiO_2, absorption and injection are dominated by $-RuP^{2+}$, followed by cross-surface electron-transfer oxidation of $-Ru^{II}-OH_2^{2+}$ (eq 6).[16] Under steady-state photolysis conditions in pH 4.5 buffer, $-Ru^{IV}=O^{2+}$ builds up at the photostationary state. The extent of surface oxidation for the co-loaded photoanode was estimated by spectral modeling (Supporting Information).

dx.doi.org/10.1021/ja505022f | J. Am. Chem. Soc. 2014, 136, 9773−9779

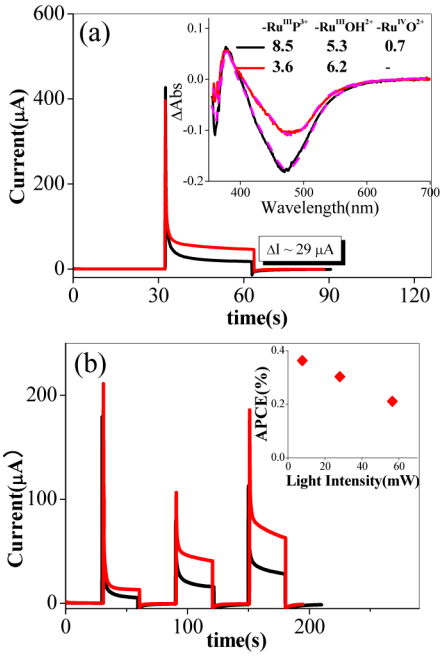

Figure 3. DSPEC current–time profiles for a TiO_2 photoanode derivatized with $Ru^{II}P^{2+}$ and $Ru^{II}OH_2^{2+}$ (5.1×10^{-8} and 6×10^{-9} mol cm^{-2}) in the absence (black) and presence (red) of 0.1 M BnOH with a 0.2 V applied bias vs NHE. Electrolyte was 20 mM pH 4.5 acetate/acetic acid buffer with 0.1 M $LiClO_4$ at room temperature. (a) 445 nm, 28.1 mW irradiation; insert: spectral changes during photoelectrolysis in the absence (black) and presence (red) of BnOH. The dashed lines in magenta are the fitted concentrations (nmol cm^{-2}) of photogenerated $-Ru^{III}P^{3+}$, $-Ru^{III}-OH^{2+}$, and $-Ru^{IV}=O^{2+}$ by spectral modeling. (b) Photocurrents at light intensities of 7.7, 28.1, and 56.5 mW; inset: APCE as a function of light intensity.

$$TiO_2-(RuP^{2+})_n,\ -Ru^{II}-OH_2{}^{2+} \xrightarrow{h\nu} TiO_2(e^-) - RuP^{3+},\ (-RuP^{2+})_{n-1},\ -Ru^{II}-OH_2{}^{2+} \rightarrow TiO_2(e^-) - (RuP^{2+})_n,\ -Ru^{III}-OH^{2+} \xrightarrow{h\nu} \cdots \rightarrow TiO_2(2e^-)-(RuP^{2+})_n,\ -Ru^{IV}=O^{2+} \quad (6)$$

The initial current–time spikes decayed rapidly to background levels, similar to results reported earlier in related photoelectrochemical cells.[7,30] On this time scale, oxidation of surface-bound Ru^{II} polypyridyl complexes is accompanied by loss of their characteristic metal-to-ligand charge transfer (MLCT) absorptions.[16] The initial photocurrents fall rapidly to the photostationary state level dictated by local interfacial dynamics-injection, back electron transfer, electron transport, proton reduction to H_2 at the cathode. For the co-loaded photoanode in the absence of BnOH there was a noticeable steady-state anodic photocurrent that appears to arise from background water oxidation but at a level that made it difficult to detect O_2 as a product.

For the co-loaded electrode on TiO_2, addition of 0.1 M BnOH resulted in an increase in steady-state photocurrent of 29 μA compared to controls with no added BnOH (Figure 3a, red). UV–vis measurements under these conditions indicates negligible $-Ru^{IV}=O^{2+}$ on the surface (Figure 3a insert). The appearance of sustained photocurrents and the absence of $-Ru^{IV}=O^{2+}$ are both consistent with BnOH oxidation at the photoanode. In an earlier study, electrocatalytic oxidation of BnOH to benzaldehyde was shown to occur following oxidation of $-Ru^{II}-OH_2{}^{2+}$ to $-Ru^{IV}=O^{2+}$ on a nanoITO electrode.[14] In the DSPEC, oxidation of BnOH at photoanodes is coupled with proton reduction to hydrogen at a Pt counter electrode with the net reaction dehydrogenation of BnOH, Scheme 1.

Scheme 1. DSPEC Diagram for Benzyl Alcohol Oxidation

Photoanode:

$$-Ru^{II}P^{2+},\ -Ru^{II}-OH_2{}^{2+} \xrightarrow{+2h\nu,-2e^-} -Ru^{II}P^{2+},\ -Ru^{IV}=O^{2+} + 2H^+$$

$$-Ru^{IV}=O^{2+} + PhCH_2OH \rightarrow -Ru^{II}-OH_2{}^{2+} + PhCHO$$

Cathode: $2H^+ \xrightarrow{+2e^-} H_2$

Net: $PhCH_2OH \rightarrow PhCHO + H_2$

Increases in steady-state photocurrents with 0.1 M added BnOH for $TiO_2-Ru^{II}P^{2+}$ and $TiO_2-Ru^{II}-OH_2{}^{2+}$ photoanodes under the same conditions were ~10 and 0.8 μA, respectively (Figure S1). The small photocurrent enhancements were expected since photogenerated $-Ru^{III}P^{3+}$ and $-Ru^{III}OH^{2+}$ are too inactive toward oxidation of the alcohol to contribute to the photocurrent.

Photocurrents for co-loaded TiO_2 scaled nonlinearly with incident light intensity. The absorbed photon to current efficiency (APCE, eq S1) was 0.36% with 7.8 mW 445 nm illumination, decreasing to 0.2% at 56.5 mW (Figure 3b insert). The efficiency drop is presumably due to rate limiting oxidation of the alcohol by $-Ru^{IV}=O^{2+}$ which is known to be relatively slow.[14] A decrease in anodic current was also observed at low $Ru^{II}P^{2+}/Ru^{II}-OH_2{}^{2+}$ ratios (<3.3) (Figure S2 and Table S1), as expected from the competing light absorption by $-Ru^{II}-OH_2{}^{2+}$ and its inefficient electron injection.[16] Multiple chromophore to catalyst loading ratios are also preferred to meet the requirement for sequential one-photon one-electron activation of the catalyst.[16]

On TiO_2, the steady-state accumulation of $-Ru^{IV}=O^{2+}$ is limited due to competition by back electron transfer with cross surface electron-transfer oxidation of $-Ru^{II}-OH_2{}^{2+}$ occurring on the hundreds of μs to ms time scale.[16] Given this, the photoelectrochemical measurements were extended to co-loaded nanoITO/TiO_2 photoanodes. Figure 4 shows the current–time profiles for nanoITO/TiO_2 photoanodes with a 0.4 V bias vs NHE in the absence of BnOH. The initial photocurrent spike decreased in the order: 4.0 nm ≈ 3.3 nm > 2.0 nm. In contrast to TiO_2, reverse, cathodic currents appeared at the end of photolysis periods. They arise from dark rereduction of photogenerated $-Ru^{III}P^{3+}$, $-Ru^{III}-OH^{2+}$, and $-Ru^{IV}=O^{2+}$ on the surface by nanoITO(e^-).

The experiments were conducted with a 0.4 V applied bias which defines the Fermi level of the nanoITO core. Back electron transfer at this potential occurs by electron tunneling from nanoITO(e^-)/TiO_2 to $-Ru^{III}P^{3+}$, $-Ru^{III}-OH^{2+}$, and $-Ru^{IV}=O^{2+}$ on the surface. From the data in Figure 4a, the extent of rereduction varies with shell thickness in the order: 2.0 nm > 3.3 nm > 4.0 nm. This observation is consistent with a decrease in electron tunneling efficiency as shell thickness increases.

With 0.1 M added BnOH, the photocurrents for co-loaded nanoITO/TiO_2–$Ru^{II}P^{2+}$,–$Ru^{II}-OH_2{}^{2+}$ with 3.3 and 4.0 nm TiO_2 shells remained at 60%–90% of the initial level (Figures 4b and S4). Under these conditions, cathodic currents at the end of the photolysis period were negligible consistent with

dx.doi.org/10.1021/ja505022f | J. Am. Chem. Soc. 2014, 136, 9773–9779

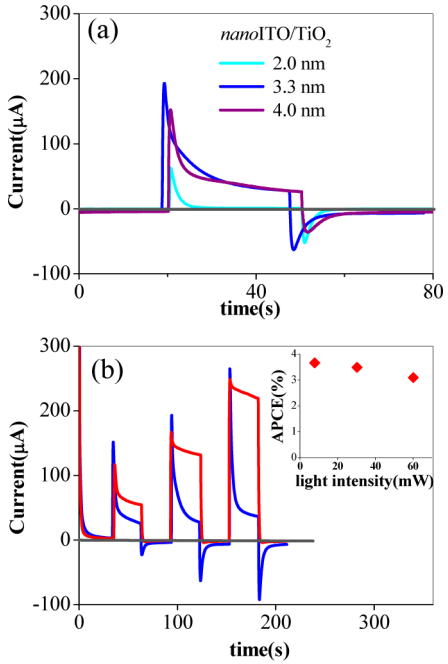

Figure 4. (a) Current−time profiles for co-loaded DSPEC, nanoITO/TiO_2−$Ru^{II}P^{2+}$, −Ru^{II}−OH_2^{2+} in the absence of BnOH with shell thicknesses of 2.0 nm (cyan), 3.3 nm (blue), and 4.0 nm (purple) under 30.3 mW, 445 nm irradiation. 0.4 V bias was applied to the photoanodes. (b) Current−time profiles for nanoITO/TiO_2−$Ru^{II}P^{2+}$, −Ru^{II}−OH_2^{2+} (9.8×10^{-9} and 1.8×10^{-9} mol cm^{-2}) with a 3.3 nm shell in the absence (blue) and presence (red) of 0.1 M BnOH under 7.8, 30.3, and 60 mW 445 nm irradiation. Insert: APCE as a function of light intensity.

reduction of photogenerated −Ru^{IV}=O^{2+} on the surface by BnOH. No sustained photocurrent was observed for −$Ru^{II}P^{2+}$ derivatized nanoITO/TiO_2 (Figure S5).

APCE values calculated from photocurrents for 3.3 nm shells was 3.7% under 7.8 mW illuminations. 3.5% and 3.1% APCE values were obtained at 30.3 and 60 mW (Figure 3b insert). A 4.0 nm shell sample showed a comparable APCE of 3.6% at 7.8 mW illumination with a 0.6 V applied bias. The photo activity of the 2.0 nm TiO_2 shell was very low (Figures S6 and S7).

When using nanoITO/TiO_2, the bias required to reach the plateau photocurrent was more positive than for TiO_2. This effect was further investigated by measuring the current−potential profiles of the two types of electrodes. Under irradiation, a decrease in photocurrent is observed as the potential was scanned from positive to negative, Figures 5 and S7. At sufficiently negative biases, depending on shell thickness, the dominant interfacial event became electron accumulation in TiO_2 or TiO_2 shells. The Guassian-shaped peaks that appear as the bias is decreased arise from electron population of trap/acceptor states in TiO_2.[52−54] Peak potentials for filling these states decrease in the order: 4.0 nm (0.04 V) > 3.3 nm (−0.034 V) > TiO_2 (−0.17 V). Such changes in trap state energy of nanoITO/TiO_2 photoanodes would require higher applied biases for proton reduction at the counter electrode, consistent with the increase in plateau potential for photocurrents upon reverse scans (Figure S7): 0 V for TiO_2, 0.2 V for the 3.3 nm shell, and 0.5 V for the 4.0 nm shell.

Photoelectrolysis for 3−5 h periods was conducted with co-loaded TiO_2 or nanoITO/TiO_2 photoanodes with 0.1 M added BnOH. Benzaldehyde was the only product in the electrolyte

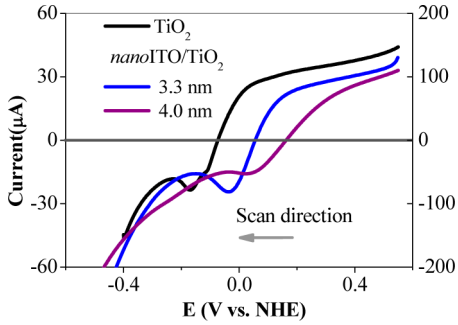

Figure 5. Current−voltage profiles during forward bias scans for TiO_2−$Ru^{II}P^{2+}$, −Ru^{II}−OH_2^{2+} (5.1×10^{-8} and 6.0×10^{-9} mol cm^{-2}, black, left axis), nanoITO/TiO_2(3.3 nm)−$Ru^{II}P^{2+}$, −Ru^{II}−OH_2^{2+} (9.8×10^{-9} and 1.8×10^{-9} mol cm^{-2}, blue, right axis), and nanoITO/TiO_2(4.0 nm)−$Ru^{II}P^{2+}$, −Ru^{II}−OH_2^{2+} (1.6×10^{-8} and 7.2×10^{-9} mol cm^{-2}, purple, right axis) under ∼29 mW 445 nm irradiation in the presence of 0.1 M BnOH in pH 4.5 buffer with 0.1 M $LiClO_4$. Complete current−voltage profiles under dark and light are shown in Figure S7.

following photolysis as detected by GC-FID consistent with the previous electrocatalytic study.[14] The Faradaic efficiency for benzaldehyde production was 26% on TiO_2 and 37% on nanoITO/TiO_2 (3.3 nm). In a parallel experiment, controlled potential electrolysis on $Ru^{II}OH_2$ derivatized nanoITO under the same conditions used in the photolysis resulted in benzaldehyde in 66% Faradaic efficiency, Table S3. Hydrogen was produced with an 87% Faradaic efficiency at the cathode (Tables S2 and S3). The lower than quantitative efficiencies for benzaldehyde production are due, in part, to competing water oxidation and decomposition of the chromophore as −$Ru^{III}P^{3+}$ (Figure S8). Loss of the chromophore inhibits further photoelectrochemical oxidation of the alcohol and the decomposition chemistry is currently under investigation.

DISCUSSION

The results presented here, and in previous reports on a nanoITO/TiO_2 core/shell-based DSSC and a water splitting DSPEC, reinforce the value of transparent conducting oxide/TiO_2 core/shell structures as an effective, tunable platform for general applications in both areas. One key of the core/shell advantage is the relatively short nm-scale transit distance from the point of injection to the conducting nanoTCO core for transfer to the underlying collector electrode compared to the micrometer distances in typical TiO_2 mesoporous films for DSSC or DSPEC applications. Core/shell composition and shell dimensions play an important role in controlling interfacial dynamics and, with them, device performance.

The estimated Fermi level for the nanoITO core in nanoITO/TiO_2 core−shells is −0.24 V vs SCE (−0.04 vs NHE).[41,42] The cores also have a sufficient acceptor level density to act as efficient electron acceptors following excitation and excited-state injection. This has been confirmed by the $\sim 10^{10}$ s^{-1} injection rate and 78% injection efficiency on nanoITO derivatized by surface-bound $Ru^{II}(bpy)_2(dcb)^{2+}$ (bpy is 2,2′-bipyridine; dcb is 4,4′-$(COOH)_2$-2,2′-bipyridine) in acetonitrile. Following injection, back electron tranfer occurs with $k \sim 8 \times 10^8$ s^{-1}.[42]

In the nanoITO/TiO_2 core/shell structure, the 2−4 nm outer TiO_2 shells introduce a barrier to electron injection into the nanoITO core, eq 3, and to back electron transfer from the core to the oxidized −$Ru^{III}P^{3+}$ chromophore, eq 5a. With an

dx.doi.org/10.1021/ja505022f | J. Am. Chem. Soc. 2014, 136, 9773−9779

excited-state potential of ∼-0.55 V vs NHE for the couple, $-Ru^{III}P^{3+}/-RuP^{2+}*$, injection into the TiO_2 shell is presumably spontaneous. From the current−voltage profile in Figure 5, on nanoITO/TiO_2 with 3.3 and 4 nm shells, trap state energies fall between −0.05 to 0.15 V, comparable to or below the nanoITO Fermi level, making electron transfer from the TiO_2 layer to the core disfavored thermodynamically.

With this energetics alignment, injection occurs largely by $-RuP^{2+}*$ tunneling to nanoITO, perhaps with participation by trap states in the TiO_2 with a component of stepwise electron transfer. Trap states may contribute to the relatively low injection efficiencies by providing a pathway for back electron transfer on the sub 10 ns time scale.

The results of the back electron-transfer dynamics study provide insight into the enhanced DSPEC photodehydrogenation efficiencies at nanoITO/TiO_2 compared to TiO_2. A distinguishing feature of the core/shell, is the decrease in back electron-transfer rate by 1−2 orders of magnitude compared to TiO_2. The TiO_2 shell acts as a blocking layer following injection into the nanoITO core, slowing electron tunneling to the surface. A decrease of this magnitude in back electron transfer opens a time window for electron transport to the underlying collector electrode. It also allows multiple oxidative equivalents to accumulate at the $-Ru^{II}-OH_2^{2+}$ catalyst site, ultimately giving reactive $-Ru^{IV}=O^{2+}$ on the surface.

The dynamic advantage of nanoITO/TiO_2 core/shells with 3.3 and 4.0 nm shells appears in DSPEC efficiencies that are enhanced by ∼10 compared to TiO_2. This is an impressive gain, given the 70% electron injection efficiency for TiO_2 with an APCE of only 0.36%. With nanoITO/TiO_2 an injection efficiency of 17% results in an APCE of 3.7%. A major deleterious factor decreasing core−shell injection efficiencies appears to be a back electron-transfer component on the sub ns time scale. As discussed above, the origin of the rapid back electron-transfer component may be from the trap sites in the TiO_2 shell.

For nanoITO/TiO_2(2.0 nm), the injection efficiency was 27% with a $t_{1/2}$ of 95 μs for back electron transfer. The low activity for BnOH oxidation was unexpected. At this thickness, the electron tunneling barrier is relatively low. Therefore, with an applied bias below the potential for surface complex redox couple, electron transfer to oxidized complexes occurs, in competition with photoanodic process. This process was much less for 3.3 and 4.0 nm TiO_2 due to the high barrier for electron tunneling.

As for the initial TiO_2 based photoelectrochemical cell reported by Honda and Fujushima,[55] and the recently described chromophore-catalyst assembly for DSPEC water splitting,[10] an applied bias is required to maximize photocurrents. It is notable that the onset bias for reaching the maximum photocurrent for the core/shell structures is shifted positively compared to TiO_2 by 0.2−0.4 V. The bias dependence arises at the microscopic level from the requirement to provide sufficient driving force for proton reduction to H_2 at the cathode. From Figure 5, the potential increment to reach photocurrent maxima in the core/shell devices appears to be correlated to conduction band/trap states energetics in the TiO_2 shells.

Although not explored in detail, the current configuration and use of the co-loaded $-Ru^{II}P^{2+}/-Ru^{II}-OH_2^{2+}$ is limited in long-term performance by the instability of $-Ru^{III}P^{3+}$ form of the chromophore and by the rate of oxidation of BnOH. Both of these limitations are under investigation in studies designed to optimize the co-loaded approach in DSPEC applications.

CONCLUSIONS

We have successfully demonstrated the photoelectrochemical dehydrogenation of benzyl alcohol based on coloading of the chromophore and the catalyst on a nanoITO/TiO_2 core/shell structure. The reaction occurs by a photoelectrochemical mechanism in which $2e^-$ oxidation of benzyl alcohol to benzaldehyde occurs at the surface of the photoanode with hydrogen generated at Pt cathode. The use of the core/shell configuration allows for the buildup of the active form of the catalyst, $-Ru^{IV}=O^{2+}$, on the surface of the TiO_2 shell. It is formed by $-Ru^{II}P^{2+}$ excitation and electron injection to give $-Ru^{III}P^{3+}$, followed by cross-surface electron-transfer activation of the catalyst. Per photon absorbed current efficiencies are enhanced on the core/shell structure relative to TiO_2 by a factor of ∼10 due to the favorable interfacial dynamics and a decrease in competitive back electron transfer. These experiments may presage a general approach for the use of chromophore-catalyst assemblies, combined with core/shell structures, to achieve solar-driven activation of hydrocarbons.

ASSOCIATED CONTENT

Supporting Information

Core/shell preparation details, characterization, spectral modeling, and additional DSPEC results. This material is available free of charge via the Internet at http://pubs.acs.org.

AUTHOR INFORMATION

Corresponding Author

tjmeyer@unc.edu

Present Address

‡Chemistry Department, Building 555, Brookhaven National Laboratory, P.O. Box 5000, Upton, NY 11973−5000

Notes

The authors declare no competing financial interest.

ACKNOWLEDGMENTS

We acknowledge funding by the Center for Catalytic Hydrocarbon Functionalization, an Energy Frontier Research Center (EFRC) funded by the U.S. Department of Energy (DOE), Office of Science, Office of Basic Energy Sciences, under award DE-SC0001298 supporting W.S. and A.K.V. The UNC EFRC: Center for Solar Fuels, an EFRC funded by the U.S. DOE, Office of Basic Energy Sciences, under award DE-SC0001011 supporting B.H.F., M.K.B., L.A., and J.J.C., is gratefully acknowledged. A.M.L. was supported under award FA9550-11-C-0028, a Department of Defense, Air Force Office of Scientific Research, National Defense Science and Engineering Graduate (NDSEG) Fellowship, 32 CFR 168a. M.D.L. was supported by the Research Triangle Solar Fuels Institute. B.K. was supported by the U.S. Department of Education through a GAANN Fellowship, award number P200A120021. The authors would like to thank the Chapel Hill Analytical and Nanofabrication Laboratory (CHANL) for atomic layer deposition and transmission electron micrographs measurements.

REFERENCES

(1) Concepcion, J. J.; House, R. L.; Papanikolas, J. M.; Meyer, T. J. *Proc. Natl. Acad. Sci. U. S. A.* **2012**, *109*, 15560.

(2) Alstrum-Acevedo, J. H.; Brennaman, M. K.; Meyer, T. J. *Inorg. Chem.* **2005**, *44*, 6802.
(3) Walter, M. G.; Warren, E. L.; McKone, J. R.; Boettcher, S. W.; Mi, Q.; Santori, E. A.; Lewis, N. S. *Chem. Rev.* **2010**, *110*, 6446.
(4) Lewis, N. S.; Nocera, D. G. *Proc. Natl. Acad. Sci. U. S. A.* **2006**, *103*, 15729.
(5) Faunce, T. A.; Lubitz, W.; Rutherford, A. W.; MacFarlane, D.; Moore, G. F.; Yang, P.; Nocera, D. G.; Moore, T. A.; Gregory, D. H.; Fukuzumi, S.; Yoon, K. B.; Armstrong, F. A.; Wasielewski, M. R.; Styring, S. *Energy Environ. Sci.* **2013**, *6*, 695.
(6) Youngblood, W. J.; Lee, S.-H. A.; Kobayashi, Y.; Hernandez-Pagan, E. A.; Hoertz, P. G.; Moore, T. A.; Moore, A. L.; Gust, D.; Mallouk, T. E. *J. Am. Chem. Soc.* **2009**, *131*, 926.
(7) Moore, G. F.; Blakemore, J. D.; Milot, R. L.; Hull, J. F.; Song, H.-e.; Cai, L.; Schmuttenmaer, C. A.; Crabtree, R. H.; Brudvig, G. W. *Energy Environ. Sci.* **2011**, *4*, 2389.
(8) Brimblecombe, R.; Koo, A.; Dismukes, G. C.; Swiegers, G. F.; Spiccia, L. *J. Am. Chem. Soc.* **2010**, *132*, 2892.
(9) Gao, Y.; Ding, X.; Liu, J.; Wang, L.; Lu, Z.; Li, L.; Sun, L. *J. Am. Chem. Soc.* **2013**, *135*, 4219.
(10) Alibabaei, L.; Brennaman, M. K.; Norris, M. R.; Kalanyan, B.; Song, W.; Losego, M. D.; Concepcion, J. J.; Binstead, R. A.; Parsons, G. N.; Meyer, T. J. *Proc. Natl. Acad. Sci. U. S. A.* **2013**, *110*, 20008.
(11) Lv, H.; Geletii, Y. V.; Zhao, C.; Vickers, J. W.; Zhu, G.; Luo, Z.; Song, J.; Lian, T.; Musaev, D. G.; Hill, C. L. *Chem. Soc. Rev.* **2012**, *41*, 7572.
(12) Chen, Z.; Concepcion, J. J.; Hull, J. F.; Hoertz, P. G.; Meyer, T. J. *Dalton Trans.* **2010**, *39*, 6950.
(13) Chen, Z.; Concepcion, J. J.; Jurss, J. W.; Meyer, T. J. *J. Am. Chem. Soc.* **2009**, *131*, 15580.
(14) Vannucci, A. K.; Hull, J. F.; Chen, Z.; Binstead, R. A.; Concepcion, J. J.; Meyer, T. J. *J. Am. Chem. Soc.* **2012**, *134*, 3972.
(15) Vannucci, A. K.; Chen, Z.; Concepcion, J. J.; Meyer, T. J. *ACS Catal.* **2012**, *2*, 716.
(16) Song, W.; Ito, A.; Binstead, R. A.; Hanson, K.; Luo, H.; Brennaman, M. K.; Concepcion, J. J.; Meyer, T. J. *J. Am. Chem. Soc.* **2013**, *135*, 11587.
(17) Treadway, J. A.; Moss, J. A.; Meyer, T. J. *Inorg. Chem.* **1999**, *38*, 4386.
(18) Ruberu, T. P. A.; Nelson, N. C.; Slowing, I. I.; Vela, J. *J. Phys. Chem. Lett.* **2012**, *3*, 2798.
(19) Fang, W.; Chen, J.; Zhang, Q.; Deng, W.; Wang, Y. *Chem.—Eur. J.* **2011**, *17*, 1247.
(20) Shimizu, K.-i.; Sugino, K.; Sawabe, K.; Satsuma, A. *Chem.—Eur. J.* **2009**, *15*, 2341.
(21) Ruther, T.; Bond, A. M.; Jackson, W. R. *Green Chem.* **2003**, *5*, 364.
(22) Angelici, R. J. *ACS Catal.* **2011**, *1*, 772.
(23) Young, K. J.; Martini, L. A.; Milot, R. L.; Snoeberger, R. C.; Batista, V. S.; Schmuttenmaer, C. A.; Crabtree, R. H.; Brudvig, G. W. *Coord. Chem. Rev.* **2012**, *256*, 2503.
(24) Farràs, P.; Maji, S.; Benet-Buchholz, J.; Llobet, A. *Chem.—Eur. J.* **2013**, *19*, 7162.
(25) Chao, D.; Fu, W.-F. *Chem. Commun.* **2013**, *49*, 3872.
(26) Chen, Z.; Vannucci, A. K.; Concepcion, J. J.; Jurss, J. W.; Meyer, T. J. *Proc. Natl. Acad. Sci. U. S. A.* **2011**, *108*, E1461.
(27) Chen, Z.; Concepcion, J. J.; Hu, X.; Yang, W.; Hoertz, P. G.; Meyer, T. J. *Proc. Natl. Acad. Sci. U. S. A.* **2010**, *107*, 7225.
(28) Tamaki, Y.; Vannucci, A. K.; Dares, C. J.; Binstead, R. A.; Meyer, T. J. *J. Am. Chem. Soc.* **2014**, *136*, 6854.
(29) Swierk, J. R.; Mallouk, T. E. *Chem. Soc. Rev.* **2013**, *42*, 2357.
(30) Zhao, Y.; Swierk, J. R.; Megiatto, J. D.; Sherman, B.; Youngblood, W. J.; Qin, D.; Lentz, D. M.; Moore, A. L.; Moore, T. A.; Gust, D.; Mallouk, T. E. *Proc. Natl. Acad. Sci. U. S. A.* **2012**, *109*, 15612.
(31) Huang, Z.; Geletii, Y. V.; Musaev, D. G.; Hill, C. L.; Lian, T. *Ind. Eng. Chem. Res.* **2012**, *51*, 11850.
(32) Listorti, A.; O'Regan, B.; Durrant, J. R. *Chem. Mater.* **2011**, *23*, 3381.
(33) O'Regan, B. C.; Durrant, J. R. *Acc. Chem. Res.* **2009**, *42*, 1799.
(34) Hagfeldt, A.; Boschloo, G.; Sun, L.; Kloo, L.; Pettersson, H. *Chem. Rev.* **2010**, *110*, 6595.
(35) Ardo, S.; Meyer, G. J. *Chem. Soc. Rev.* **2009**, *38*, 115.
(36) Brennaman, M. K.; Patrocinio, A. O. T.; Song, W.; Jurss, J. W.; Concepcion, J. J.; Hoertz, P. G.; Traub, M. C.; Murakami Iha, N. Y.; Meyer, T. J. *ChemSusChem* **2011**, *4*, 216.
(37) Concepcion, J. J.; Jurss, J. W.; Norris, M. R.; Chen, Z.; Templeton, J. L.; Meyer, T. J. *Inorg. Chem.* **2010**, *49*, 1277.
(38) Chen, Z.; Concepcion, J. J.; Luo, H.; Hull, J. F.; Paul, A.; Meyer, T. J. *J. Am. Chem. Soc.* **2010**, *132*, 17670.
(39) Tong, L.; Inge, A. K.; Duan, L.; Wang, L.; Zou, X.; Sun, L. *Inorg. Chem.* **2013**, *52*, 2505.
(40) Duan, L.; Bozoglian, F.; Mandal, S.; Stewart, B.; Privalov, T.; Llobet, A.; Sun, L. *Nat. Chem.* **2012**, *4*, 418.
(41) Alibabaei, L.; Farnum, B. F.; Brennaman, M. K.; Kalanyan, B.; Losego, M. D.; Parsons, G. N.; Meyer, T. J. *Nano Lett.* **2014**, *14*, 3255.
(42) Farnum, B. H.; Morseth, Z. A.; Lapides, A. M.; Rieth, A. J.; Hoertz, P. G.; Brennaman, M. K.; Papanikolas, J. M.; Meyer, T. J. *J. Am. Chem. Soc.* **2014**, *136*, 2208.
(43) Gillaizeau-Gauthier, I.; Odobel, F.; Alebbi, M.; Argazzi, R.; Costa, E.; Bignozzi, C. A.; Qu, P.; Meyer, G. J. *Inorg. Chem.* **2001**, *40*, 6073.
(44) Lee, S.-H. A.; Abrams, N. M.; Hoertz, P. G.; Barber, G. D.; Halaoui, L. I.; Mallouk, T. E. *J. Phys. Chem. B* **2008**, *112*, 14415.
(45) Hoertz, P. G.; Chen, Z.; Kent, C. A.; Meyer, T. J. *Inorg. Chem.* **2010**, *49*, 8179.
(46) Hanson, K.; Brennaman, M. K.; Ito, A.; Luo, H.; Song, W.; Parker, K. A.; Ghosh, R.; Norris, M. R.; Glasson, C. R. K.; Concepcion, J. J.; Lopez, R.; Meyer, T. J. *J. Phys. Chem. C* **2012**, *116*, 14837.
(47) Nelson, J. *Phys. Rev. B* **1999**, *59*, 15374.
(48) Nelson, J.; Haque, S. A.; Klug, D. R.; Durrant, J. R. *Phys. Rev. B* **2001**, *63*, 205321.
(49) Nelson, J.; Chandler, R. E. *Coord. Chem. Rev.* **2004**, *248*, 1181.
(50) Barzykin, A. V.; Tachiya, M. *J.Phys. Chem. B* **2002**, *106*, 4356.
(51) Shalom, M.; Albero, J.; Tachan, Z.; Martínez-Ferrero, E.; Zaban, A.; Palomares, E. *J.Phys. Chem. Lett.* **2010**, *1*, 1134.
(52) Bisquert, J.; Fabregat-Santiago, F.; Mora-Seró, I.; Garcia-Belmonte, G.; Barea, E. M.; Palomares, E. *Inorg. Chim. Acta* **2008**, *361*, 684.
(53) Luo, H.; Song, W.; Hoertz, P. G.; Hanson, K.; Ghosh, R.; Rangan, S.; Brennaman, M. K.; Concepcion, J. J.; Binstead, R. A.; Bartynski, R. A.; Lopez, R.; Meyer, T. J. *Chem. Mater.* **2013**, *25*, 122.
(54) Ondersma, J. W.; Hamann, T. W. *J. Am. Chem. Soc.* **2011**, *133*, 8264.
(55) Fujishima, A.; Honda, K. *Nature* **1972**, *238*, 37.